

Study of the fields of the Mu2e Solenoids

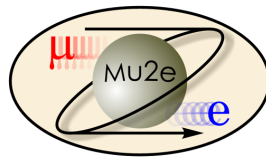
FERMILAB *Summer Student Program, 2015*

FEDERICA BRADASCIO

University of Pisa, Italy

Supervisor:

COSTAS VELLIDIS



September 25, 2015

Abstract

The Fermilab Mu2e experiment aims at exploring physics beyond the Standard Model by seeking direct muon to electron conversion in the field of a nucleus, with a sensitivity approximately four orders of magnitude better than the current world's best limits for this process. The magnet system for this experiment is made of three superconducting solenoids: the Production Solenoid (PS), the Transport Solenoid (TS) and the Detector Solenoid (DS). The field of each magnet is modeled at the points of a 3D grid, called field map. This report focuses on the comparisons of the maps produced by two different constructors: the Fermilab Technical Division and the General Atomics. Split coil model is compared with respect to the helical model for DS. In addition to the field map comparisons, a test of TS field is simulated using a $^{90}\text{Sr}/^{90}\text{Y}$ β^- source. Using two different field maps, uncertainties of up to ~ 200 G in the end of TS are introduced in the simulation. The test is insensitive to these field differences.



CONTENTS

I Mu2e Experiment	1
II The solenoids	3
I Production Solenoid	3
II Transport Solenoid	4
III Detector Solenoid	5
III Coordinate Systems	5
IV The field maps	6
I The tools	7
II Comparisons	8
V Simulations of electron source test of TS field	13
VI Conclusions	20

I. MU2E EXPERIMENT

The Mu2e experiment [1] at Fermilab proposes to measure the ratio of the rate of the neutrinoless, coherent conversion of muons into electrons in the field of a nucleus, relative to the rate of ordinary muon capture on the nucleus:

$$R_{\mu e} = \frac{\mu^- + A(Z, N) \rightarrow e^- + A(Z, N)}{\mu^- + A(Z, N) \rightarrow \nu_\mu + A(Z - 1, N)}.$$

The conversion process is an example of charged lepton flavor violation (CLFV), a process that has never been observed experimentally. The current best experimental limit on muon-to-electron conversion, $R_{\mu e} < 7 \times 10^{-13}$ (90%CL), is from the SINDRUM II. Mu2e intends to probe four orders of magnitude beyond the SINDRUM II sensitivity, measuring $R_{\mu e}$ with a single-event sensitivity of 2.87×10^{-17} .

The conversion of a muon to an electron in the field of a nucleus is coherent: the muon recoils off the entire nucleus and the kinematics are those of two-body decay. The mass of a nucleus is large compared to the electron mass so the recoil terms are small. A conversion electron is therefore monoenergetic with energy slightly less than the muon rest mass:

$$E_e = m_\mu c^2 - B_\mu(Z) - C(A)$$

where Z and A are the number of protons and nucleons in the nucleus, $B_\mu(Z)$ is the atomic binding energy of the muon and $C(A)$ is the nuclear recoil energy. In the case of muonic aluminum, the energy of the conversion electron is 104.97 MeV and the muon lifetime is 864 ns. An electron of this energy signals the conversion.

At the proposed Mu2e sensitivity there are a number of processes that can mimic a muon-to-electron conversion signal. Controlling these potential backgrounds drives the overall design of Mu2e. These backgrounds result principally from five sources:

1. intrinsic processes that scale with beam intensity; these include muon decay-in-orbit (DIO) and radiative muon capture (RMC);
2. processes that are delayed because of particles that spiral slowly down the muon beam line, such as antiprotons;
3. prompt processes where the detected electron is nearly coincident in time with the arrival of a beam particle at the muon stopping target (e.g. radiative pion capture, RPC);
4. electrons or muons that are initiated by cosmic rays;
5. events that result from reconstruction errors induced by additional activity in the detector from conventional processes.

To achieve the sensitivity goal cited above a high intensity, low energy muon beam coupled with a detector capable of efficiently identifying 105 MeV electrons while minimizing background from conventional processes is required.

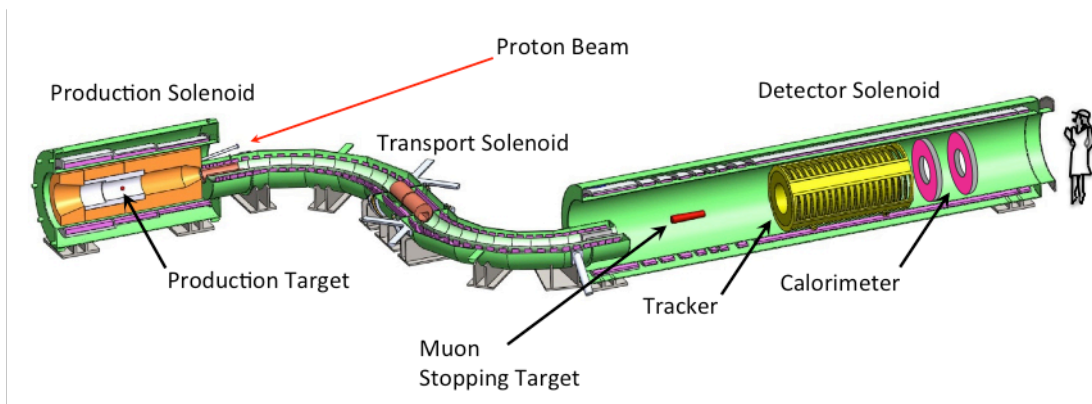


Figure 1: The Mu2e muon beamline showing the positions of the primary proton beam, the three solenoids, the production target, the stopping targets, and the detectors.

The Mu2e experimental apparatus (see [Figure 1](#)) consists of an integrated array of superconducting solenoids, which forms a graded magnetic system that includes the Production Solenoid (PS), the Transport Solenoid (TS) and the Detector Solenoid (DS).

The experiment proceeds in three main steps:

1. The muon beam is created by an 8 GeV proton beam (delivered by the Fermilab accelerator complex) striking a gold production target in PS; interactions in the target produce pions that subsequently decay to muons.

2. The low energy negatively charged muon are transmitted from PS to the stopping target in DS by S-shaped Transport Solenoid. Negatively charged particles with high energy, positively charged particles and line-of-sight neutral particles are nearly all eliminated by absorbers and collimators before reaching the Detector Solenoid.
3. The muon beam is then delivered to the stopping target, a set of thin aluminium foils in DS. DIO and conversion electrons from the stopping targets are transported to the spectrometer in a graded magnetic field. The momentum of these electrons is measured, with a resolution of about 150 keV/c, in a tracker; a calorimeter gives an independent measurement of position and energy. The calorimeter has poorer energy resolution than does the tracker but it helps to reject backgrounds arising from badly reconstructed tracks.

The tracking detector is made from low mass straw tubes oriented transverse to the solenoid axis. The momentum resolution is dominated by fluctuations in the energy lost in the stopping target and proton absorber, by multiple scattering, and by bremsstrahlung of the electron in the tracker. The calorimeter consists of about 1900 crystals arranged in two disks oriented transverse to the solenoid axis. The calorimeter provides timing and energy information important for providing a fast trigger and efficient particle identification.

II. THE SOLENOIDS

The solenoids perform several critical functions for the Mu2e experiment. Magnetic fields generated from these magnets are used to efficiently collect and transport muons from the production target to the muon stopping target while minimizing the transmission of other particles. Electrons are transported from the stopping target to detector elements where a uniform and precisely measured magnetic field is used to measure the momentum of electrons. The magnetic field values range from a peak of 4.6 T at the upstream end to 1 T at the downstream end. In between is a complex field configuration consisting of graded fields, toroids and a uniform field region, each designed to satisfy a very specific set of criteria.

Mu2e creates this complex field configuration through the use of three magnetically coupled solenoid systems: Production Solenoid (PS), the Transport Solenoid (TS) and the Detector Solenoid (DS).

I. Production Solenoid

The Production Solenoid is a high field magnet with a graded solenoidal field varying smoothly from 4.6 Tesla to 2.5 Tesla. The gradient will be formed by 3 axial coils with a decreasing number of windings, made of aluminum stabilized NbTi. The solenoid is approximately 4 m long with an inner bore diameter of approximately 1.5 m that is evacuated to 10^{-5} Torr.

The Production Solenoid is designed to capture pions and the muons into which they decay and guide them downstream to the Transport Solenoid. This process is initiated by 8 GeV protons striking a production target near the center of the Production Solenoid. Remnant protons that are not absorbed by the target and very forward-produced secondary particles exit at the high field end of the solenoid. Pions in the forward direction with angles greater than $\sim 30^\circ$, relative to the

solenoid axis, are reflected back by the higher field and move along with the backward produced particles in helical trajectories towards the Transport Solenoid.

II. Transport Solenoid

The S-shaped Transport Solenoid consists of a set of superconducting solenoids and toroids that form a magnetic channel that efficiently transmits low energy negatively charged muons from the Production Solenoid to the Detector Solenoid. Negatively charged particles with high energy, positively charged particles and line-of-sight neutral particles are nearly all eliminated by absorbers and collimators before reaching the Detector Solenoid. Selection of negatively charged muons is accomplished by taking advantage of the fact that a charged particle beam traversing a toroid will drift perpendicular to the toroid axis, with positives and negatives drifting in opposite directions. Most of the positively charged particles are absorbed in the central collimator.

The Transport Solenoid consists of five distinct regions: a 1 m long straight section (TS1), a 90° curved section (TS2), a second straight section about 2 m long (TS3), a second 90° curved section (TS4) that brings the beam back to its original direction, and a third straight section (TS5) of 1 m length. The major radius of the two curved sections is about 3 m and the resulting total magnetic length of the Transport Solenoid along its axis is about 13 m. The inner warm bore of the Transport Solenoid cryostat has a diameter of about 0.5 m. The Transport Solenoid is shown in [Figure 2](#).

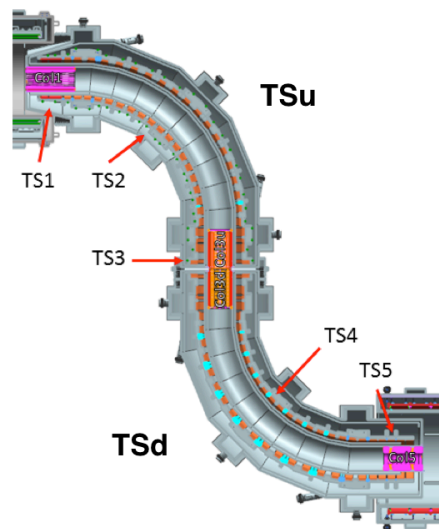


Figure 2: *The Transport Solenoid consists of a set of superconducting solenoid and toroids that form a magnetic channel that efficiently transmits low energy negatively charged muons from the Production Solenoid.*

Particles produced with a small pitch in a uniform field region can take a very long time to progress down the beamline toward the muon stopping target. To suppress background from these late arriving particles, the three straight sections in the Transport Solenoid employ negative

axial gradients for radii smaller than 0.15 m. The radius is set by the geometry of the beam collimators. This requirement is intended to eliminate traps, where particles bounce between local maxima in the field until they eventually scatter out and travel to the Detector Solenoid where they arrive late and may cause background.

The requirement on a negative gradient is relaxed in the curved sections of the TS because they are toroidal sections. In fact in a toroid region, spiraling particles drift up or down depending on the sign of their charge, with a displacement that is proportional to their momentum and inversely proportional to their pitch. Particles with small pitch progress slowly through the toroid and drift to the wall where they are absorbed.

III. Detector Solenoid

The Detector Solenoid is a large, low field magnet that houses the muon stopping target and the detectors required to identify and analyze conversion electrons from the stopping target. It is nearly 11 m long with a clear bore diameter of about 2 m. The muon stopping target resides in a graded field that varies from 2 T to 1 T. On the TS side of the muon stopping target, the graded field captures conversion electrons that are emitted in the direction opposite the detector components causing them to reflect back towards the detector. On the other side of the stopping target, the graded field focuses electrons toward the tracker and calorimeter. The graded field also plays an important role in reducing background from high energy electrons that are transported to the Detector Solenoid by steadily increasing their pitch as they are accelerated towards the downstream detectors. The resulting pitch angle of these beam electrons is inconsistent with the pitch of a conversion electron from the stopping target.

The actual detector components reside in a field region that is relatively uniform. The field in this region has two requirements. First, the magnetic field is important for the measurement of the electron momentum and energy. The tracker-determined trajectory, along with the magnetic field map, determines the electron momentum. This requires the magnetic field to be as uniform as possible. The tracker-determined trajectory is then extrapolated into the downstream calorimeter and matched with calorimeter energy deposition. The energy/momentum match further validates the electron identification. The second design consideration is that local field minima are a potential source of backgrounds. This background is reduced by superimposing a small negative axial gradient in the tracker and calorimeter region.

III. COORDINATE SYSTEMS

Figure 3 shows the Mu2e coordinate systems.

(X, Y, Z) The Mu2e global cartesian system centered in the middle of TS. In PS and DS the z coordinate is aligned to the magnetic axis.

(u, y, s) Coordinate system attached to the Mu2e axis, with the s axis tangent to the symmetry axis (i.e., for PS and DS, parallel to the Z axis in the Mu2e coordinate system), the y axis pointing vertical up (i.e. parallel to the Y axis in the Mu2e coordinates everywhere), and the u axis completing a right-handed cartesian system. In PS and DS, this local system is simply

parallel-translated w.r.t. the global Mu2e system in the XZ-plane, to have the origin on the Mu2e symmetry axis. In TS, it is both translated and rotated in the XZ-plane. In TS3, the positive u axis becomes parallel to the Mu2e positive Z axis and the positive s axis becomes parallel to the Mu2e negative X axis.

(s, r, Φ) The s is defined as above, r is the coordinate transverse to s and Φ is the rotation angle (azimuth) around the axis. Φ is defined so that $\Phi = 0$ corresponds to the $+u$ axis.

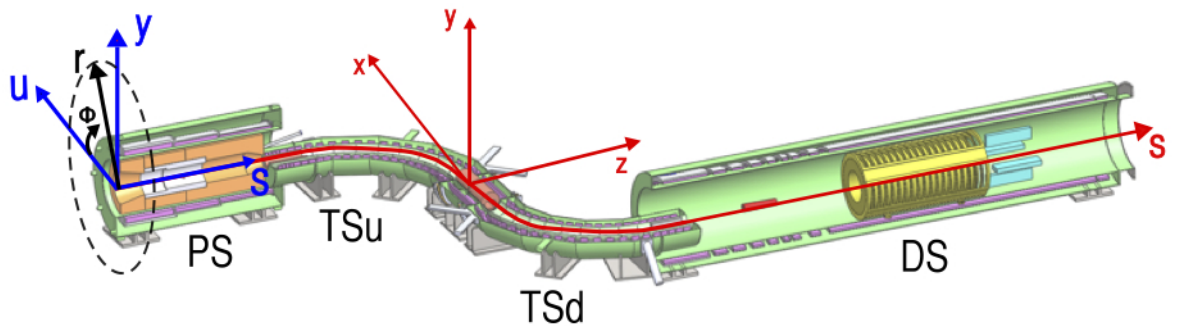


Figure 3: The Mu2e coordinate systems: the (u, y, s) local cartesian system (in blu), the (r, Φ, s) cylindrical system (in black) and the (x, y, z) Mu2e global cartesian coordinate system (in red), centered in the middle of the TS.

IV. THE FIELD MAPS

The Mu2e experiment is based on a complex of superconducting solenoid magnets, which form a graded magnetic system. In order to do simulations at first and run the experiment later, it is necessary to know as accurately as possible the magnetic field in the volumes where particles are transported or detected. The magnetic field of each magnet is mapped at the points of a 3D grid, which is called *Field Map*.

The Mu2e solenoids will be built by two different constructors: PS and DS will be built by the *General Atomics (GA)*, while the TS will be built by the *Technical Division (TD)* of Fermilab. Consequently we have two set of maps and we want to test them by direct comparisons of fields. Therefore, two sets of maps are used in the simulations, one set from each constructor.

The field maps provided by TD (labeled *Mau9*) are the default set of maps for current simulation in Mu2e Offline software. They describe all magnets as solenoids; they assume the XZ-plane symmetry and consequently are one-sided maps (field values given only at points for $Y \geq 0$). To

expand the maps for negative Y , the field is reflected w.r.t. the XZ-plane using:

$$\begin{aligned} B_x(X, -Y, Z) &= B_x(X, Y, Z) \\ B_y(X, -Y, Z) &= -B_y(X, Y, Z) \\ B_z(X, -Y, Z) &= B_z(X, Y, Z) \end{aligned}$$

Different field maps have been provided by GA (labeled with a number which states the version): GA00, GA01, GA02, GA03, GA04. They differ in the XZ-plane symmetry assumption (one-sided if symmetry is assumed, two-sided if not) and model of DS magnet (split or helical coils). Table 1 lists all the GA field maps and their properties.

Table 1: List of GA field maps. GA00 is the equivalent to the Mau9 maps, used as benchmark for the Null Test (checks if the fields are numerically identical at all points of the grid). The one-sided maps give field values just for $Y \geq 0$ (assuming XZ-plane symmetry), while double-sided maps are given for positive, zero and negative Y . DS coils can be split (solenoid model) or helical (helical winding model).

	GA00	GA01	GA02	GA03	GA04
Map extension	Double-sided	One-sided	Double-sided	Double-sided	Double-sided
DS Coils	Split	Split	Split	Helical	Helical

I. The tools

In order to compare the field maps of the Mu2e solenoids, I developed a set of Root tools. They are designed to use two sets of maps, where each set has a map for each solenoid (PS, TSu, TSd, DS). Each set may or may not assume XZ-plane symmetry and, depending on the assumption, it is used accordingly.

ContourTool.C

This module is designed to make plots of the field components B_x , B_y , B_z and of the field gradient $\frac{dB}{ds}$ on a circle centered at a given point on the Mu2e symmetry axis, specified by the input path length S (> 0) and of a given radius r . The field components and the field gradient are plotted as a function of the arc length L along the circle. The field components are interpolated at the points on the circle using trilinear interpolation. The gradient is approximated by a 2-point difference ratio. This tool contains geometry functions which make transformations from the local coordinate system (u, y, s) to the Mu2e coordinate system (x, y, z) and back and from the local cartesian to the cylindrical system (r, Φ, s) and back.

EasyTest.C

This module is designed to scan all grid points in a given set of field maps and do calculations with the input field, which are written in an output text file. The module writes the coordinates, field components, field magnitude and field gradient dB/ds along paths parallel to the Mu2e symmetry axis at 4 azimuthal angles about the axis: 0, 90, 180, and 270 degrees. The paths are drawn across Mu2e, starting from the upstream entrance of PS ($S=0$) and ending at the downstream exit of DS,

at input-specified radii. If requested, the module can also produce an output text file containing the coordinates and the field magnitude at exactly all points of the grid, without interpolation.

test_maps.C

This module is designed to make plots of the results from `EasyTest.C`, computed along paths parallel to the $\text{Mu}2e$ axis. It produces the following:

- table of relative differences of the field components and gradient;
- plots of comparisons of field components along the path;
- plots of comparisons of field magnitude and derivative vs path length;
- histograms of field absolute component differences along the path;
- histograms of field relative component differences along the path.

test_grid.C

This module is designed to make plots of the results from `EasyTest.C` on the grid points, without interpolation. It creates:

- plots of the histograms of $\log_{10} |B(\text{map}2) - B(\text{map}1)|$ and $\log_{10} \left| \frac{B(\text{map}2) - B(\text{map}1)}{B(\text{map}1)} \right|$, in logarithmic scale of the axis of entries;
- scatter plots of points where $\text{dB} = |B(\text{map}2) - B(\text{map}1)|$ is above an input-specified threshold. The coordinate of the points in the scatter plots are defined in the (u, y, s) and (r, Φ, s) systems.

II. Comparisons

Using the tools described above, I make numerical comparisons between the field maps provided by GA and TD. The first step is to compare the GA maps which use the DS solenoid model (i.e. GA00, GA01, GA02) with Mau9 maps: this is the benchmark (*Null Test*) because we expect to find differences well below the design tolerance ($\leq 10^{-4}$), since both the maps use the same magnetic model. The two sets of maps should agree at this level of precision for the GA helical model to be reliable. After the Null Test, if GA with DS split coils is found consistent with Mau9, it will be used as reference for other comparisons with the GA maps assuming DS helical model.

The comparisons made are:

1. GA01 vs Mau9 (1st Null Test) [2];
2. GA03 vs Mau9 (1st Helical Test) [3];
3. GA03 vs GA02 (2nd Helical Test) [4];
4. GA00 vs Mau9 (2nd Null Test) [5];
5. GA04 vs GA00 (3rd Helical Test) [6];

The first three numerical comparisons revealed inconsistencies between Mau9 and GA calculations, eventually traced to the fact that the two maps had a few coils in slightly different positions. For this reason GA provided two more maps with the inconsistencies fixed: GA00, used for Null Test with Mau9 maps, and GA04, identical to Mau9 except new DS model, which has to be compared with GA00.

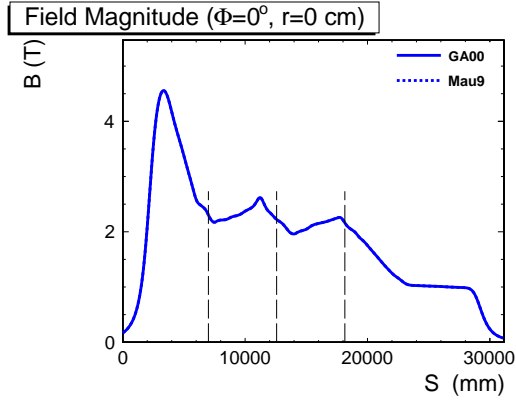
Each comparison is made using the plots and tables produced by the the Root tools described above:

- plots of the magnetic field components, magnitude and gradient at $\Phi = 0^\circ, 90^\circ, 180^\circ, 270^\circ$ and radii from 0 to 90 cm in steps of 5 cm around the Mu2e symmetry axis;
- histograms of absolute differences of the magnetic field components, in linear and decimal logarithm scale, at the various Φ and radii;
- histograms of logarithmic absolute and relative differences of the field magnitude at all grid points;
- numerical tables of relative differences of field components and of field gradients.

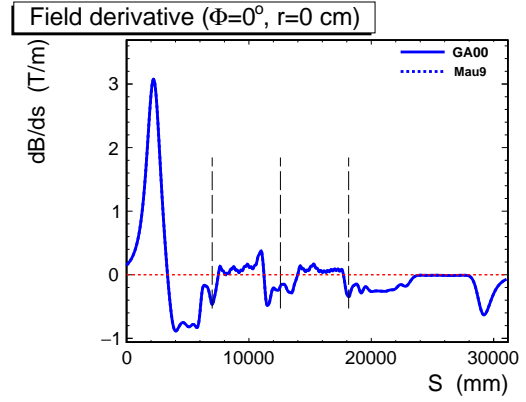
Figure 4 shows plots for the GA00 vs Mau9 comparison: results are shown on the magnetic axis, along all the path length S (from the entrance of PS through the exit of DS). The dotted vertical lines denote, from left to right, the boundaries between PS, TSu, TSd and DS. The flat segments in the DS region in 4(a) correspond to the detector fiducial volume, where the field has to be uniform in order to analyze the momentum of the conversion electrons; the same region is evident in 4(b), where the derivative is 0. The 4(d) histograms point out that the bigger differences are in the TS region. Investigations of the plots at finite radii showed that they are most prominent close to the coils ($r=40$ cm) at the TS boundaries. Absolute differences are generally observed at the level of 10^{-4} , except in the TS region near the coils where they go up to the level of $10^{-2.5}$.

From the highest bin of the logarithmic histogram (4(d)) we can inspect how strong the largest differences are. We can look for the grid points where the largest differences occur, using scatter plots in the (u, y, s) and (r, Φ, s) local coordinate systems. Figure 5 shows the scatter plots for the DS magnet: no differences are observed in the fiducial volume, so that there are no effects on physics. The main significant differences (> 1 G) in $|B|$ are detected near the coils: this is probably associated with details of numerical integration.

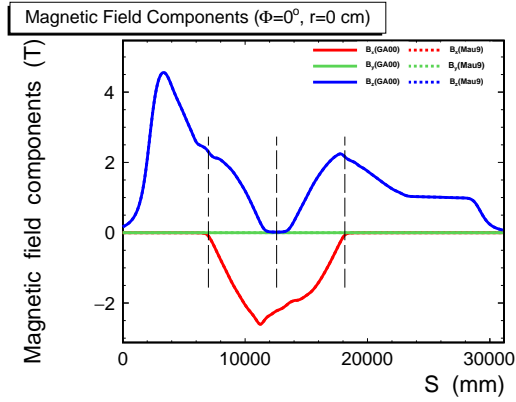
Figure 6 shows comparisons between the GA00 and GA04. Overall consistency between the two calculations is observed, except in the DS region. These differences are expected because of the different DS model (split coils in GA00, helical coil in GA04). The biggest difference is observed (6(d)) near the exit of DS where the field drops to zero, pointing to a slightly different turn-off curve.



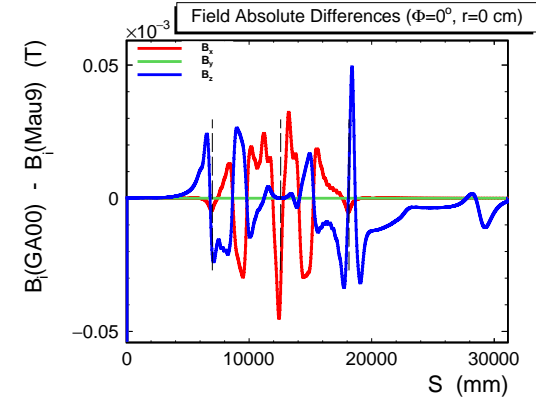
(a) Comparisons of the magnitude of the magnetic field as functions of the path length s . The flat area in the DS region corresponds to the detector fiducial volume.



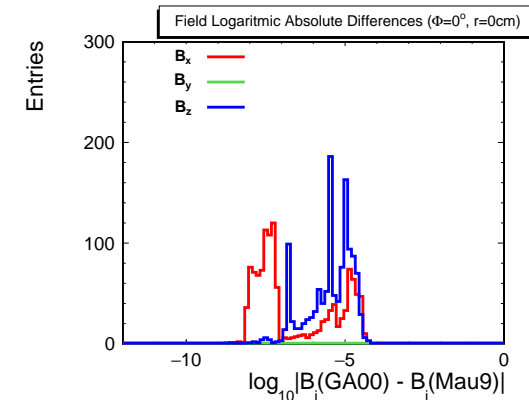
(b) Comparisons of the derivative of the magnetic field with respect to and as function of the path length s . The 0 derivative area in the DS region corresponds to the detector fiducial volume.



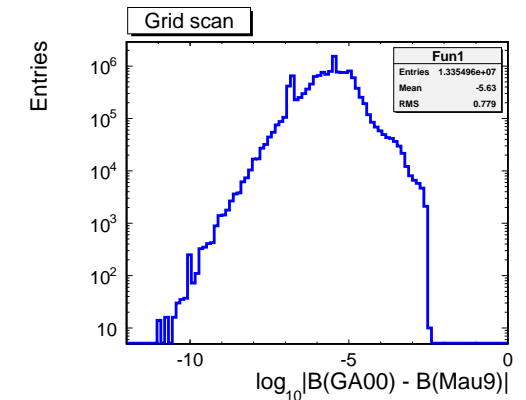
(c) Comparisons of the magnetic field components as functions of the path length.



(d) Histogram of the absolute differences of the magnetic field components.



(e) Histogram of the decimal logarithm of the absolute differences of the magnetic field components.



(f) Histogram of logarithmic absolute differences of the field magnitude at all grid points.

Figure 4: Comparisons between Mau9 and GA00 (Null Test) field maps, on the magnetic axis, along all the path length S (from the entrance of PS through the exit of DS). Dotted vertical lines denote the boundaries of PS, TSu, TSd and DS regions.

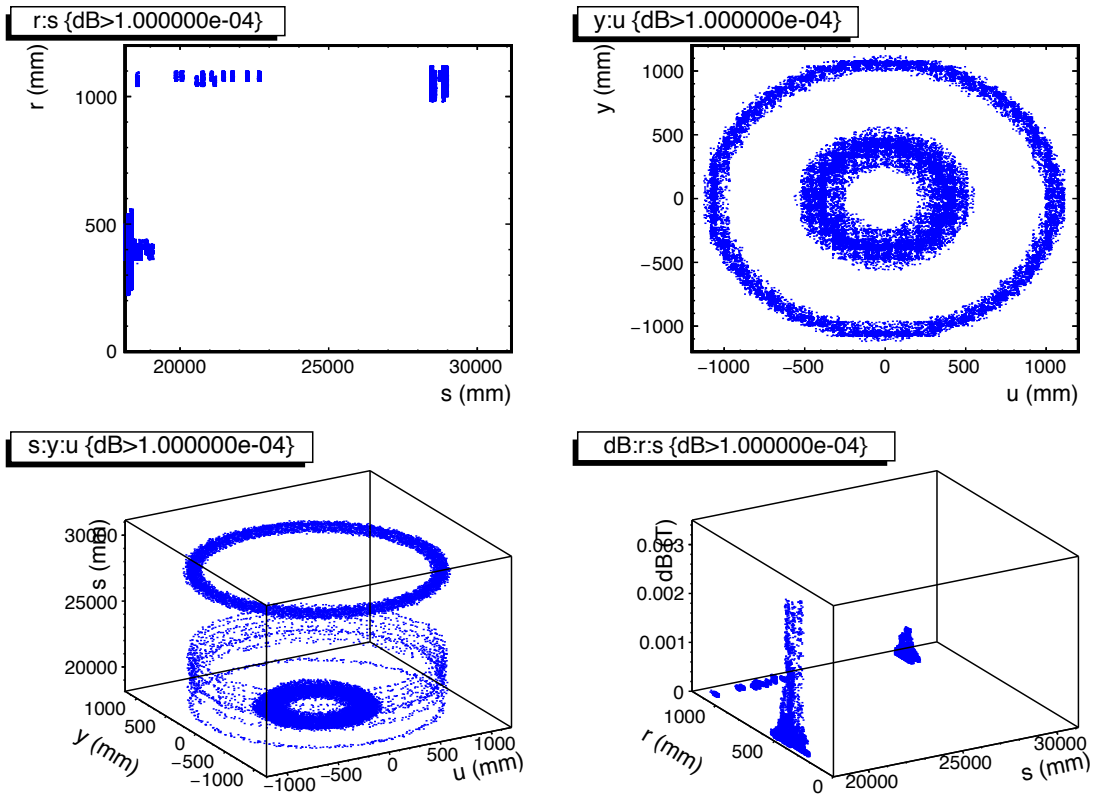
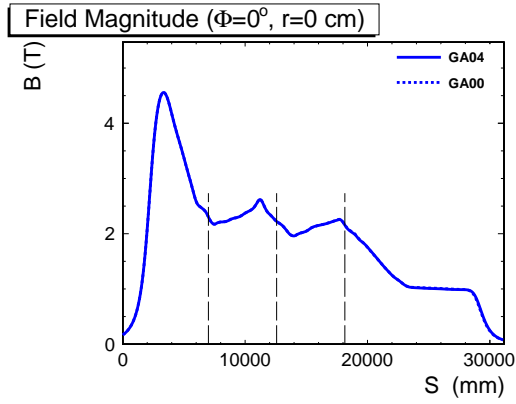
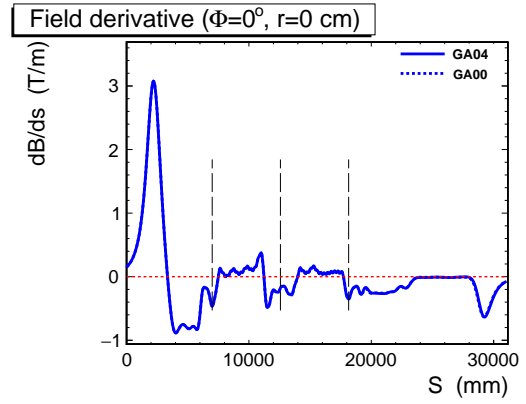


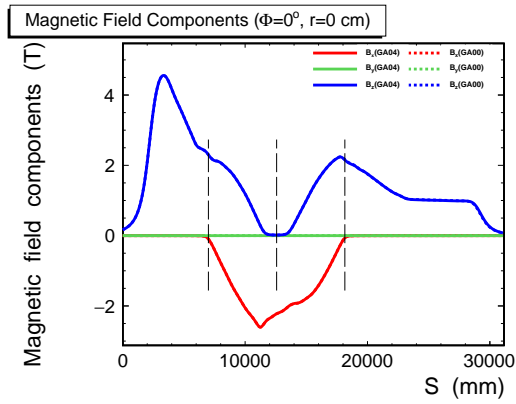
Figure 5: Scatter plots of DS grid points where the field magnitude differs by more than 1 G between the GA00 and the Mau9 DS maps. The coordinate systems used are (u, y, s) and (r, Φ, s) .



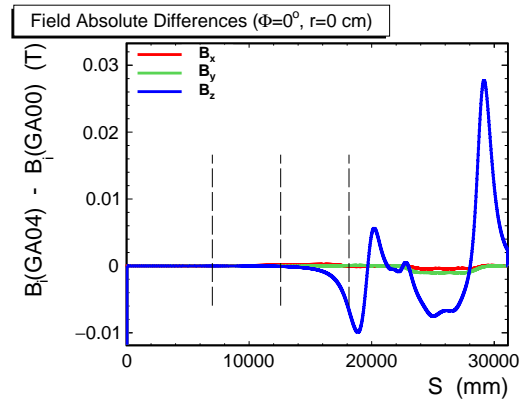
(a) Comparisons of the magnitude of the magnetic field as functions of the path length s .



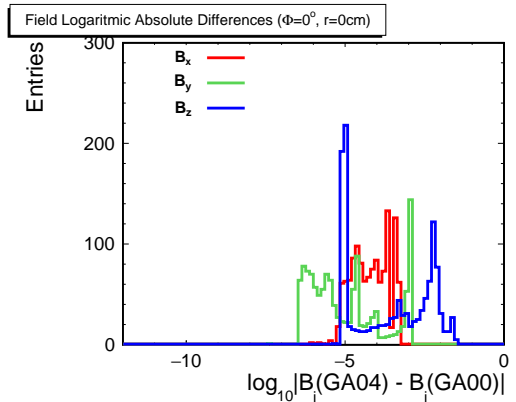
(b) Comparisons of the derivative of the magnetic field with respect to and as function of the path length s .



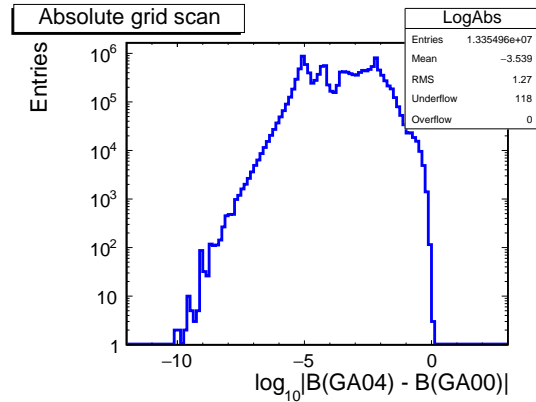
(c) Comparisons of the magnetic field components as functions of the path length.



(d) Histogram of the absolute differences of the magnetic field components.



(e) Histogram of the decimal logarithm of the absolute differences of the magnetic field components.



(f) Histogram of logarithmic absolute differences of the field magnitude at all grid points.

Figure 6: Comparisons between GA00 and GA04 field maps, on the magnetic axis, along all the path length s (from the entrance of PS through the exit of DS).

V. SIMULATIONS OF ELECTRON SOURCE TEST OF TS FIELD

After the solenoid system commissioning will be completed, the magnetic field of the solenoids has to be mapped. While the field of PS and DS solenoids will be measured using field probes, the same is not possible for TS because of the complicated design of the support system. An alternative possible solution is to use a commercial source of charged particles (electrons) emitted into the TS field. The principle of the test is that low momentum electrons follow paths very close to the field lines, and thus they can help trace the field if they are detected at various positions inside the solenoids. They can also be used to check the geometry constraints (apertures, absorber foils, collimators).

The electron source could be a beta or electron conversion isotope with electron or positron energies up to a few MeV. Preliminary studies [7] have shown that the best tradeoff among sufficient momentum range, moderate source activity (to suppress hazard) and lack of background particles (e.g. photons) is $^{90}\text{Sr}/^{90}\text{Y}$. Figure 7 shows the characteristic of this source.

Activity	0.1 μCi ^a
Half-lifetime	28.79 years
Emissions	100% (β^- , β^-)
Decay max Energy	546 keV, 2280 keV

^a 1 μCi = 37,000 decays/s	
---	--

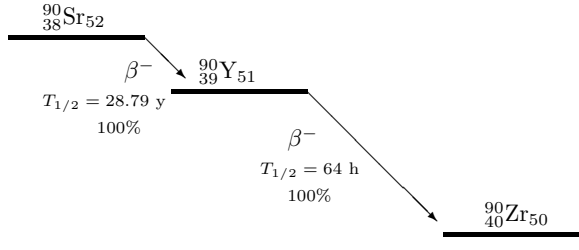


Figure 7: β^- decay of the ^{90}Sr into ^{90}Y , which decays into an electron and ^{90}Zr .

The choice of the detector is driven by the precision requirements of the test, that are high efficiency and uniform response. A solution proposed is a system of scintillator tiles directly coupled to multi-pixel photon counters (MPPC), without fibers to guide the light, studied by the Northern Illinois University and Fermilab for an ILC high-segmentation hadron calorimeter. It consists of square or hexagonal scintillator tiles of area of 9 cm² and thickness of 5 mm, concave on the one side at a depth of 3 mm, with a spherical cavity corresponding to a radius of 15 mm.

The β^- test is simulated using the ART framework: 50000 electrons are generated by the $^{90}\text{Sr}/^{90}\text{Y}$ isotope. The source is shifted to various x-y positions relative to the solenoid axis (local cartesian system): the z position is fixed to -6000 mm (in front of the production target location), while y changes from 0 to 50 and 100 mm and x to -50 mm and 50 mm from the axis. The phase space allowed to the electrons is $0^\circ < \theta < 8^\circ$ wrt the z axis. Six virtual detectors (VD) are used in the positions shown in Figure 8: each pair of VD surrounds one collimator window. There are two detectors in the entrance of TS1, two before and two after the p-bar absorber in TS3 and the last two in the very end of TS5. The simulation traces the path of the electrons only along TS. The vacuum pressure is set to 1 Torr, so that multiple scattering processes are allowed. The simulation was repeated twice with two different field maps (Mau9 and GA01), as a way to simulate uncertainties of the field at the commissioning phase. Eventually, varied maps from TD will be used, incorporating field variations from random displacements of the coils.

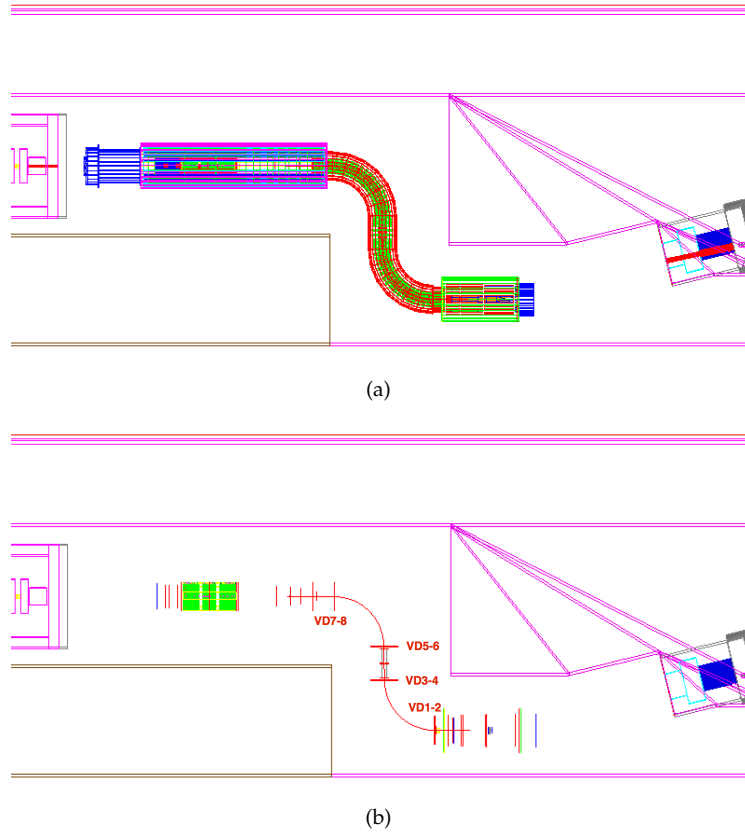


Figure 8: Plan view of the Mu2e hall for the β^- test simulation, with Ps on the lower right and DS on the upper left. In 8(b) the cryostats and the coils are invisible so that the inside of the beam line and the position of the virtual detectors are visible. The electron track is the red line on axis.

Figure 9 and Figure 10 show the $^{90}\text{Sr}/^{90}\text{Y}$ spectrum: in the first figure the source is on the axis, in the second one it is shifted in $(x, y, z) \equiv (3954, 100, -6000)$. The spectrum is the convolution of the ^{90}Sr and ^{90}Y spectra: in 9(a) the first peak corresponds to ^{90}Sr , the second one to ^{90}Y . When the source is on axis there are no changes in momentum in the various virtual detectors. When we move from the axis (Figure 10) the spectrum remains the same as long as the particles are in TSu (i.e. VD1, VD2, VD3, VD4), but after passing the TS3 collimator only the high momentum peak is visible (10(b)), because the low momentum particles have been absorbed and cut by the p -bar window in TS3. Note that the number of entries decreases as we go through the exit of TS because some particles are scattered.

Figure 11 and Figure 13 show 2D histograms of local y vs x for all virtual detectors, when the β^- source is on the axis and in $(x, y, z) \equiv (3954, 100, -6000)$. Scatter plots for source on axis and off axis are shown in Figure 12 and Figure 14: the scale of the plots is quite different because as we move into TS the magnetic field changes the trajectory of the particles. Moreover, the pressure allows scattering on air so that there are outliers in the last virtual detectors.

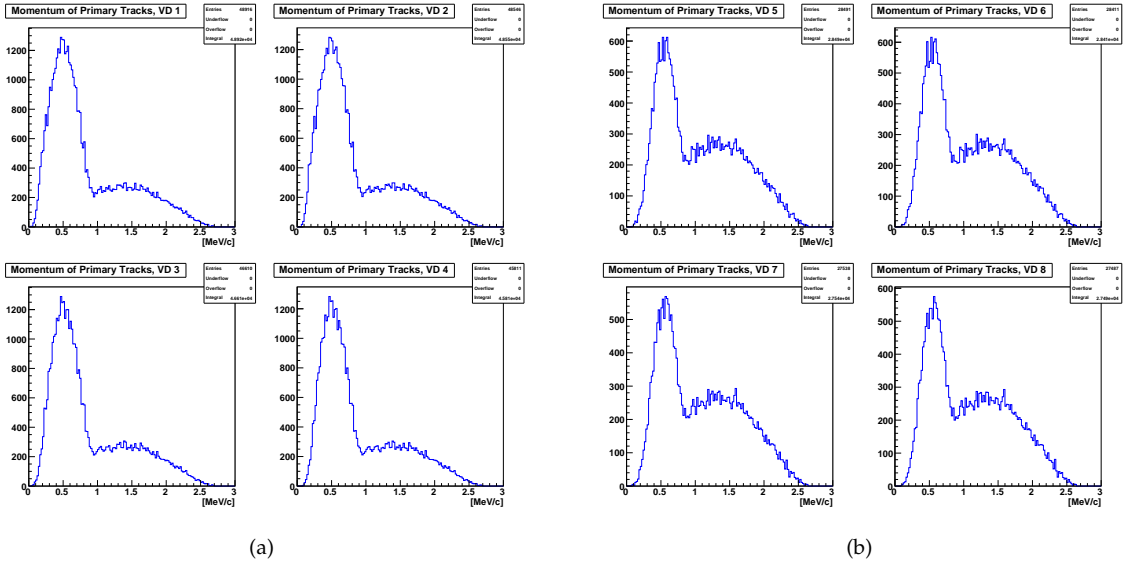


Figure 9: Plots of the momentum spectrum in the eight virtual detectors, with the β^- source in $(x, y, z) \equiv (3954, 100, -6000)$ in the Mu2e global system. The spectrum is the convolution of the ^{90}Sr and ^{90}Y spectra: in 10(a) the first peak corresponds to ^{90}Sr , the second one to ^{90}Y . There are no changes in the momentum in the various virtual detectors: the low momentum particles are not cut by the collimators.

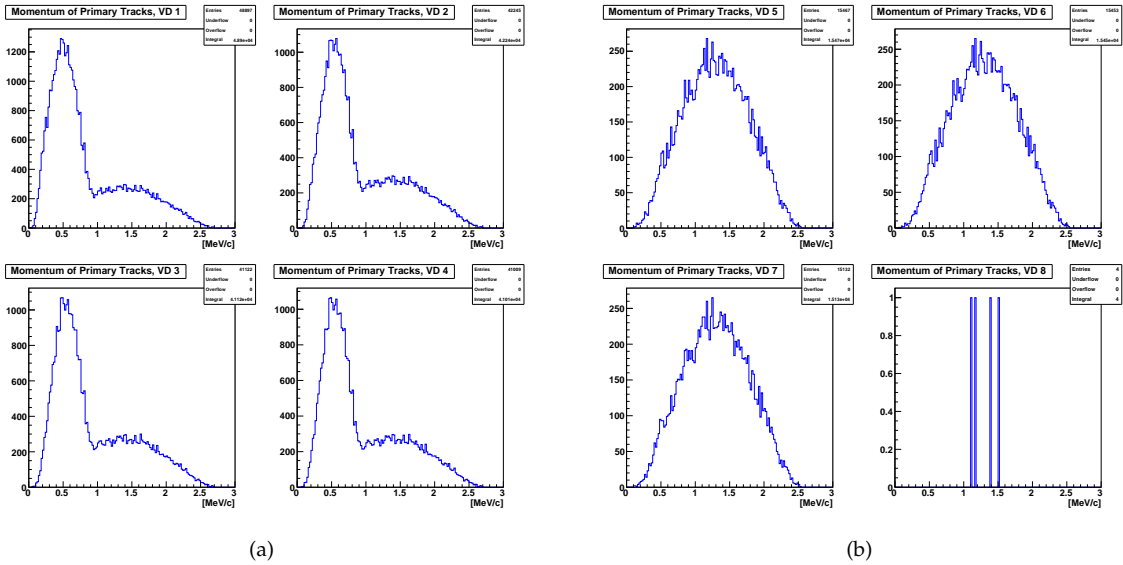
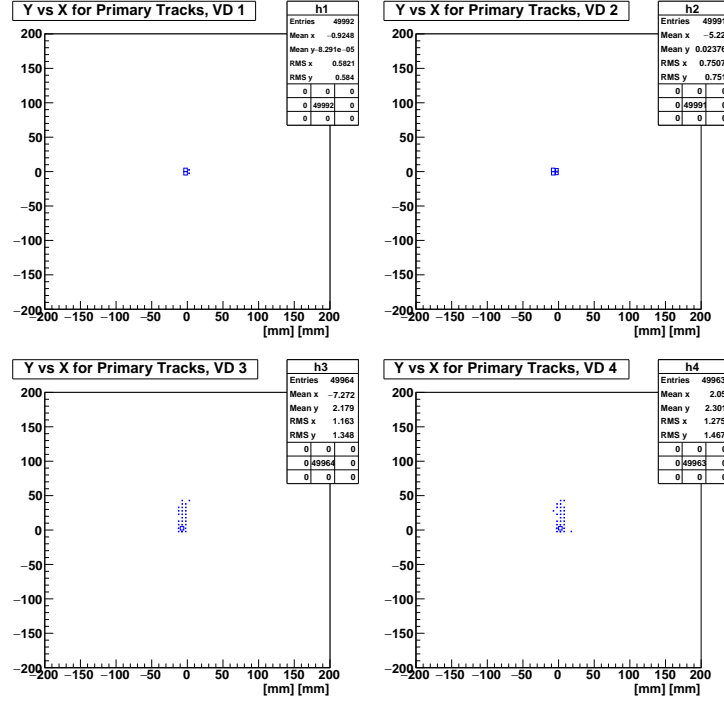
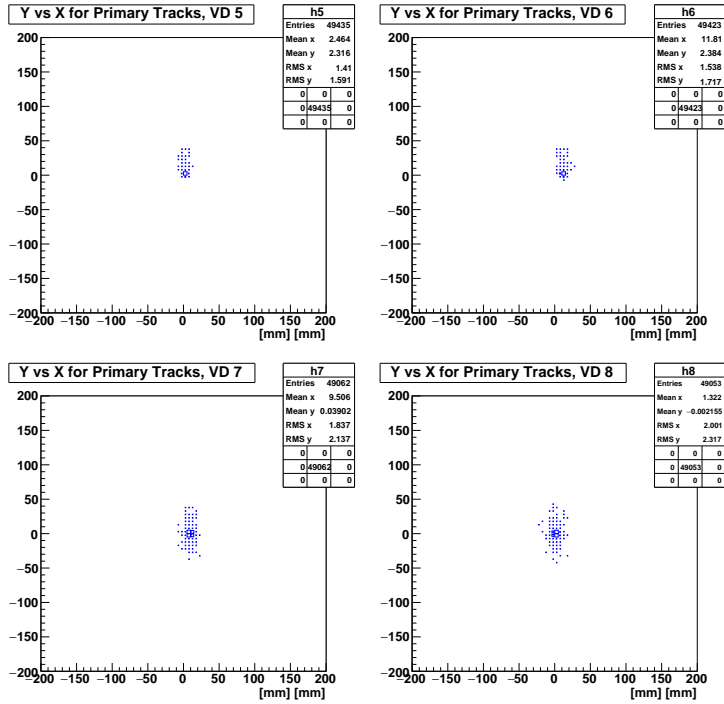


Figure 10: Plots of the momentum spectrum in the eight virtual detectors, with the β^- source in $(x, y, z) \equiv (3954, 100, -6000)$ in the Mu2e global system. The spectrum is the convolution of the ^{90}Sr and ^{90}Y spectra: in 10(a) the first peak corresponds to ^{90}Sr , the second one to ^{90}Y . Figure 10 shows that there are no changes in the momentum in TSu (i.e. VD1, VD2, VD3, VD4): only the number of entries decreases because some particles have been scattered. After VD5 (10(b)) there is only the pick of the higher momentum particles, because the low momentum particles have been absorbed in TS3.

Figure 11: 2D histograms of local y vs x for the 8 virtual detectors. The β^- source is on axis: $(x, y, z) \equiv (3904, 0, -6000)$.

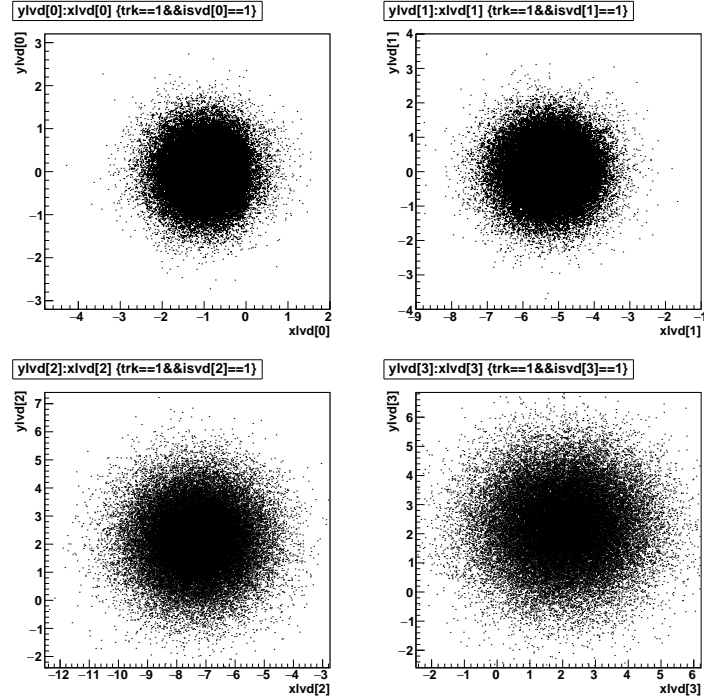


(a)

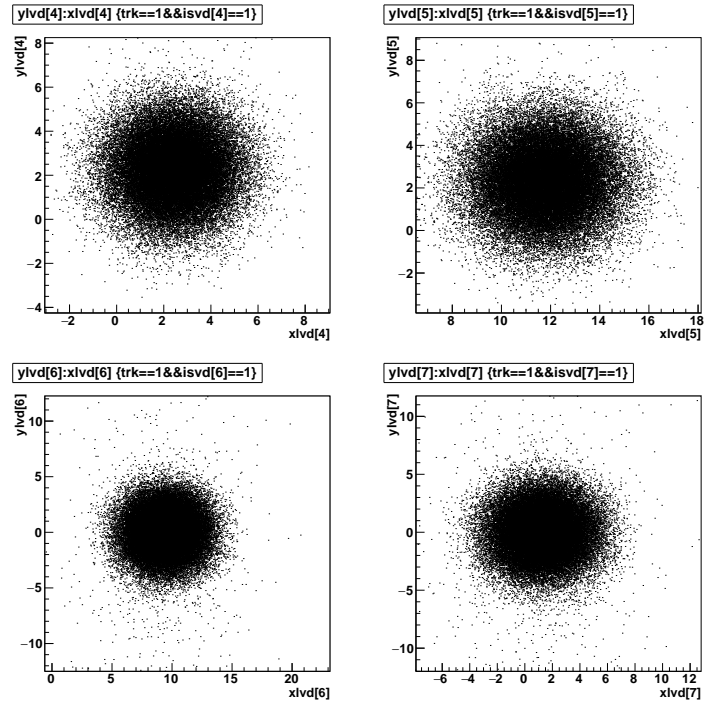


(b)

Figure 12: Scatter plots (13(a), 13(b)) for the eight virtual detectors, with the β^- source on the axis. In 15(a) and 15(b) the scale is quite different because of the design of the field, which changes the particle trajectories, and the presence of outliers (scatter effects due to the air in the solenoid bore).

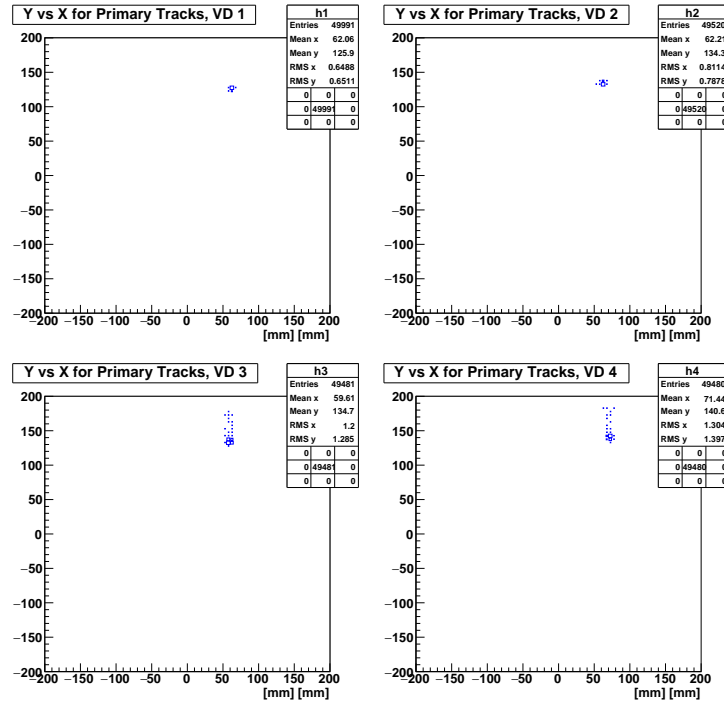


(a)

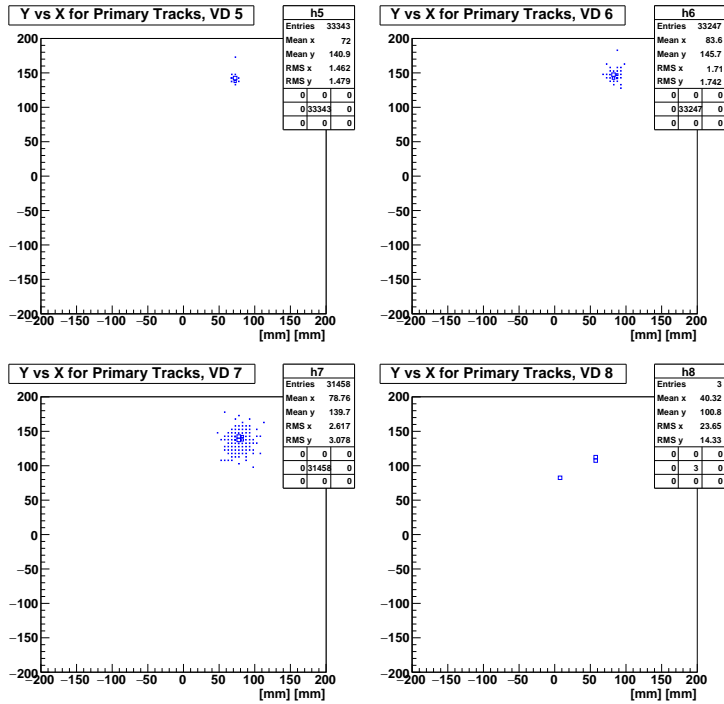


(b)

Figure 13: 2D histograms of local y vs x for the 8 virtual detectors. The β^- source is in $(x, y, z) \equiv (3954, 100, -6000)$.

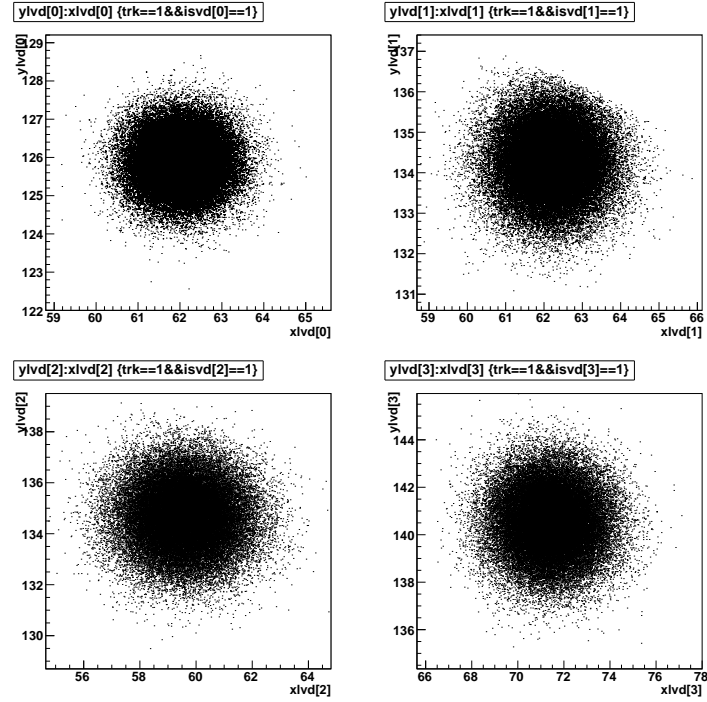


(a)

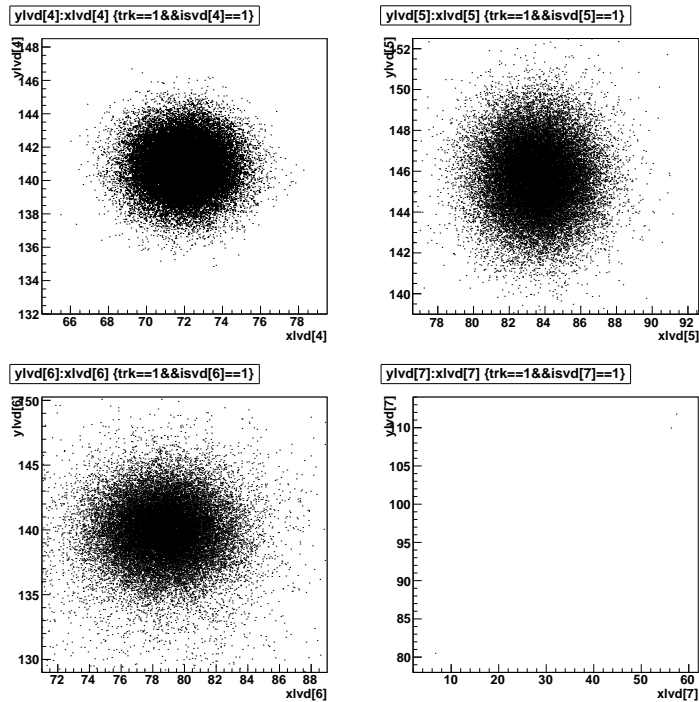


(b)

Figure 14: Scatter plots (15(a), 15(b)) of the particles in the eight virtual detectors, with the β^- source in $(x, y, z) \equiv (3954, 100, -6000)$ in the Mu2e global system. In 15(a) and 15(b) the scale is quite different because of the design of the field, which changes the particles trajectories, and the presence of outliers (scatter effects due to the air in the solenoid bore). For these reasons just a few particles are seen by the last detector.



(a)



(b)

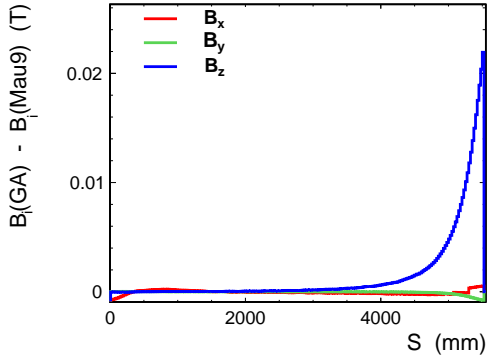


Figure 15: Histogram of absolute differences between Mau9 and GA01 in TSd.

The simulation was run twice, at first using Mau9 and then the GA01 field maps for TSd and DS (PS and TSu were still from the Mau9 set). GA01 maps were chosen because, from the comparisons described in the previous sections, it resulted to have the biggest differences wrt Mau9 field maps. The simulation does not show any differences using the two maps. As it can be seen in Figure 15, GA01 differs from Mau9 maps by up to ~ 200 G close to the exit of TS: thus the β^- test is insensitive to uncertainties of this order at the end of solenoid.

VI. CONCLUSIONS

Methods and Root tools for precision testing of the Mu2e design magnetic fields have been developed. TD Mau9 field maps have been compared with those provided by General Atomics. Inconsistencies between the two sets of maps have been identified in the first numerical comparisons, but they have been fixed by GA, which provided new maps. The Null Test revealed good agreement between benchmark maps: GA00 matched Mau9 to 10^{-4} in fiducial volume. Overall consistency between GA00 and GA04, except in DS, was found in the subsequent helical test: the differences in DS could be understood by the change in the design (from split coils to helical coils).

A preliminary simulation to test the TS field using a β^- source model has been made. A complete scan to trace the electron paths in TS was performed by moving the β^- source in 9 different positions (changing x and y coordinates). The simulation was run twice using two different field maps: uncertainties of the order of up to ~ 200 G in the exit of TS have no effects on the results of the test.

REFERENCES

- [1] Mu2e Collaboraton, *Mu2e Technical Design Report*, arXiv:1501.05241
- [2] Federica Bradascio, *Comparisons of Null Test GA and Default Mu2e Offline Field Maps*, Mu2e-doc-5865
- [3] Federica Bradascio, *Comparisons of Helical Winding GA and Default Mu2e Offline Field Maps*, Mu2e-doc-5888
- [4] Federica Bradascio, *GA Helical Model vs Null Test Field Map Comparisons*, Mu2e-doc-5957
- [5] Federica Bradascio, *Comparisons of New Null Test GA00 and Default Mu2e Offline Field Maps Mau9*, Mu2e-doc-5999

- [6] Federica Bradascio, *Comparisons of GA00 and GA04 Field Maps*, Mu2e-doc-6025
- [7] Costas Vellidis, *Electron Test for the Mu2e Transport Solenoid Field*, Mu2e-doc-4617